JOC The Journal of Organic Chemistry

Article

pubs.acs.org/joc

Study of Model Systems for Bilirubin and Bilin Chromophores: Determination and Modification of Thermal and Photochemical Properties

Cristina García-Iriepa,[‡] Hanna A. Ernst,[§] Yu Liang,[§] Andreas-Neil Unterreiner,[§] Luis Manuel Frutos,[‡] and Diego Sampedro*[,†]

[†]Departamento de Química, Centro de Investigación en Síntesis Química (CISQ), Universidad de La Rioja, Madre de Dios 53, E-26006 Logroño, Spain

[‡]Unidad Docente de Química Física, Universidad de Alcalá, Alcalá de Henares, E-28871 Madrid, Spain

[§]Institute of Physical Chemistry, Karlsruhe Institute of Technology (KIT), 76128 Karlsruhe, Germany

Supporting Information

ABSTRACT: Bilin chromophores and bilirubin are involved in relevant biological functions such as light perception in plants and as protective agents against Alzheimer and other diseases. Despite their extensive use, a deep rationalization of the main factors controlling the thermal and photochemical properties has not been performed yet, which in turn hampers further applications of these versatile molecules. In an effort to understand those factors and allow control of the relevant properties, a combined experimental and computational study has been carried out for diverse model systems to understand the interconversion between *Z* and *E* isomers. In this study, we have demonstrated the crucial role of steric hindrance and hydrogen-bond interactions in thermal stability and the ability to control them by designing novel compounds. We also determined several photochemical properties and studied the photodynamics of two model systems in more detail, observing a fast relaxation of the excited state shorter than 2 ps in both cases. Finally, the computational study allowed us to rationalize the experimental evidence.

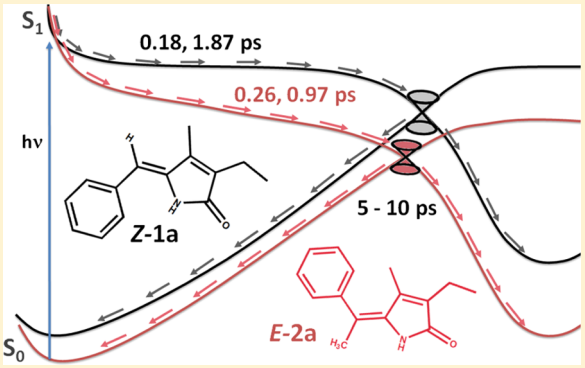

INTRODUCTION

Photoisomerization of carbon−carbon double bonds is a common mechanism in biological processes. The different biological activities and properties of *Z* and *E* isomers lead to diverse functions and responses.[1−5] Taking advantage of this, the use of light has been extensively employed in different therapies, so-called phototherapies, as a way to control the *Z*/*E* isomer ratios of certain chromophores with quite different biological cytotoxicities.[6−9] Well-known chromophores that involve *Z*/*E* photoisomerizations in nature are the retinal chromophore in rhodopsins, which controls the process of vision,[2,10] and the green fluorescent protein (GFP) chromophore,[4,11,12] extensively applied as a reporter gene and fluorescent probe.

Another large and heterogeneous family of *Z*/*E* photoswitchable biomolecules is phytochromes, photoreceptors present not only in plants but also in some bacteria and fungi.[13,14] These proteins consist of two major structural domains, the globular *N*-terminal chromophore-binding domain (65 kDa) and the structurally open *C*-terminal domain. The photoactive part includes a bilin chromophore with an open tetrapyrrolic system in which the rings are connected by methine units, leading to a structure with extended conjugation (see Figure 1A).[15]

This chromophore can be interconverted between two different states, the dark-stable, red-absorbing isomer P_r and the metastable far-red-absorbing isomer P_{fr}. Upon exposure to light (λ_{max} = 660 nm), P_r undergoes photoisomerization of one exocyclic carbon−carbon double bond followed by proton transfer, leading to P_{fr} (λ_{max} = 730 nm), which is usually the physiological active isomer.[16] The biological output, P_r/P_{fr} ratio, depends not only on the ambient light but also on the photochemical reaction kinetics and the thermal (dark) reversion process.[17,18] This photoisomerization leads to a reversible conformational change of the protein,[19] which constitutes the first step of the phytochrome-signaling cascade. This basic system allows for the regulation of several functions such as seed germination or photomorphogenesis in plants[20] or growth, development, and pigmentation in bacteria.[21−24]

In humans, bilin chromophores are metabolic products of some porphyrins, such as bilirubin, whose chemical structure is very similar to those of bilin pigments (see Figure 1B).[25−27]

Received: April 20, 2016
Published: July 8, 2016

DOI: 10.1021/acs.joc.6b00892
J. Org. Chem. 2016, 81, 6292−6302

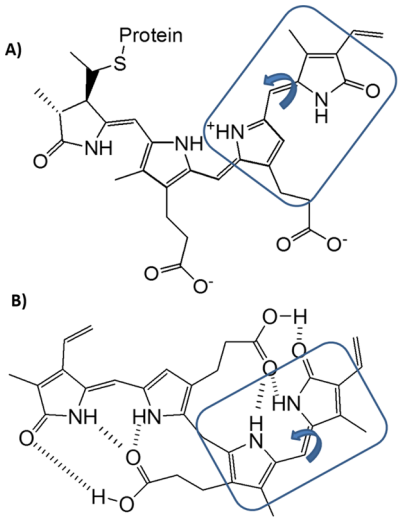

Figure 1. Structures of (A) phytochrome and (B) bilirubin chromophores. The photoisomerizable double bonds and their corresponding model systems are depicted.

The study of the photophysical and photochemical properties of bilirubin is of special interest as its elevated levels are related to diverse diseases such as neonatal jaundice among others. Phototherapy is the treatment most used against this affliction.[28−30] Similarly to bilin chromophores, an exocyclic carbon−carbon double bond of the dark stable *ZZ* isomer photoisomerizes to the metastable *ZE* isomer after irradiation.[31] This photoproduct presents a more polar chemical structure, as some of the hydrogen bonds present in the *ZZ* isomer are disrupted, facilitating its excretion across the liver to the bile.[31,32]

The study of model systems of photoswitchable biological chromophores is an approach extensively applied to understand the properties of the natural analogues. For instance, the penta-2,4-dieniminium cation and 4-(4-hydroxybenzylidene)-1,2-dimethyl-1*H*-imidazol-5(4*H*)-one have been used in numerous studies as model systems of the retinal[33,34] and the GFP chromophores,[35−38] respectively. Concerning the phytochrome chromophore and bilirubin, dipyrrinone[39,40] and benzalpyrrolinone[41,42] derivatives (see Figure 2) are the most studied models.

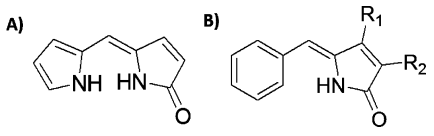

Figure 2. Structures of (A) dipyrrinone and (B) benzalpyrrolinone derivatives.

Thus, while the biological relevance of phytochrome and bilirubin is well-known and their biochemical features broadly studied, more information is still needed to better understand the basic functioning of these systems. With this aim, we focused on the rationalization of the structural parameters that can modify several relevant properties. First, we studied the thermal properties of benzalpyrrolinone analogues and proposed a novel model system where the vinylic hydrogen has been replaced by a methyl group. Moreover, as the formation of hydrogen-bond interactions in bilin pigments plays an important role in phototherapy, we have evaluated the strength of hydrogen-bond interactions, rationalized the effect of this stabilization energy on the relative thermal stability of both isomers, and demonstrated their effect on the photochemical properties (e.g., UV−vis spectra, photoisomerization extent). Furthermore, in order to better understand the biological processes, we aimed to figure out the photoisomerization dynamics and mechanism of two representative models. The dynamic processes that take place during the photoisomerization were studied by UV−vis transient absorption spectroscopy (TAS). In addition, a computational study was performed to investigate the geometry of the ground-state minima, the photoisomerization mechanism and the hydrogen bond effect in the excited state. The data collected allowed us to rationalize the properties of these model systems and provide valuable information for the more complex biological systems.

RESULTS

Synthesis and Thermal Properties. First, benzalpyrrolinone derivatives (compounds **1a−j**) were synthesized following the method of Chepelev et al.[39] (see Scheme 1A). The selected

Scheme 1

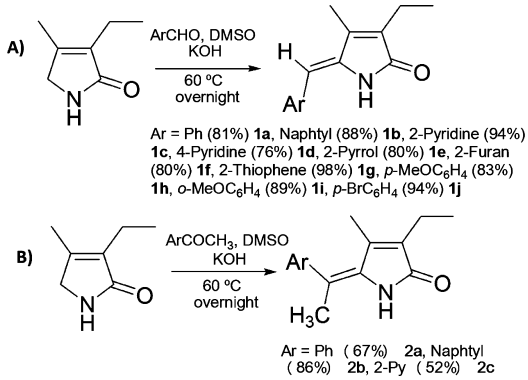

aldehyde and 3-ethyl-4-methyl-1,5-dihydropyrrol-2-one were dissolved in DMSO, and the solution was sparged with nitrogen. Then a solution of KOH in water was added, and the solution kept overnight at 60 °C (see the Experimental Section). Moreover, we have synthesized a novel family of benzalpyrrolinones with a methyl group instead of a hydrogen atom in the vinylic position (compounds **2a−c**). The experimental procedure was similar to the one described above, but the aldehyde is replaced by a ketone (see Scheme 1B).

In most of the synthesized compounds, just one isomer was obtained in the reaction crude. The configuration of the central carbon−carbon double bond of the most thermally stable isomer was elucidated by NOE experiments (see the Supporting Information). For compounds **1a−j**, the *Z* isomer is the thermally stable isomer, similar to other benzalpyrrolinone analogues,[43,44] whereas the *E* isomer is the most thermally stable for compounds **2a**,**b**, and a mixture of both isomers was obtained in the synthesis of compound **2c** (see Figure 3). Hence, the replacement of the vinylic hydrogen by a methyl group has a clear and direct effect on the thermal stability.

As mentioned in the Introduction, the presence of hydrogen-bond interactions is crucial for these systems, controlling the biological activity and photoisomerization degree. Therefore, we have studied the formation and strength of hydrogen-bond

DOI: 10.1021/acs.joc.6b00892
J. Org. Chem. 2016, 81, 6292−6302

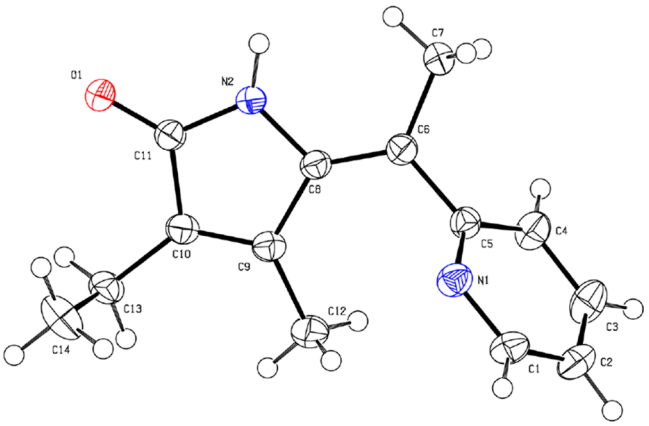

Figure 3. X-ray structure of compound *E*-**2c** with thermal ellipsoids shown at 50% probability.

interactions for compounds **1a**–**j**. According to this thermal property, derivatives **1a**–**j** can be classified into three groups: (i) monomers without hydrogen bond, (ii) monomers with an intramolecular hydrogen bond, and (iii) dimers with an intermolecular hydrogen bond.

In order to stablish the monomer/dimer structure and the possibility of hydrogen-bond interaction, ^{1}H NMR, DOESY, and X-ray data were recorded and analyzed (see the Supporting Information). Compounds **1a**,**b**,**h**–**j** are monomers that cannot lead to hydrogen-bond interactions (group i) due to the lack of NH or OH groups in the aryl moiety. In the case of compound **1d** (4-Py), although an intermolecular hydrogen-bond interaction could be possible, the X-ray structure (CCDC-1457874, see Figure S2A) and the ^{1}H NMR chemical shift of the amide proton (δ_{NH} $CDCl_3$ = 8.82 ppm, see the Supporting Information) discard this hypothesis (at the concentration used for the characterization).

It has been previously reported that compound **1e** (Ar = pyrrole) is a dimer due to intermolecular hydrogen-bond interaction (group ii)[45] and that compounds **1c**,**f**,**g** present an intramolecular hydrogen bond (group iii).[43] However, the strength of the hydrogen-bond interactions in compounds **1c**,**f**,**g** has never been analyzed, and it is crucial in order to understand both the thermal and photochemical properties. To do this, the monomer vs dimer structure was checked for compounds **1c**,**f**,**g** by DOSY experiments (see the Supporting Information) due to their similar structure compared to **1e**. The hydrodynamic volume ratio, compared to the pyrrole derivative (**1e**), is ca. 2 (see Table 1), indicating that compounds **1c**,**f**,**g** are monomers.

Once the monomer structure of compounds **1c**,**f**,**g** was set, we evaluated their ability to establish intramolecular hydrogen-bond interaction and their strength. With this goal in mind, we analyzed the amide proton chemical shift variation from $CDCl_3$ to DMSO-d_6 ($\Delta\delta$) and its temperature dependence ($\Delta\delta/\Delta T$) (see Table 1 and the Supporting Information). As can be observed in Table 1, the chemical shift of the amide proton is almost invariant with the solvent for compound **1c**, whereas for compounds **1f** and **1g** it changes 1.30 and 2.12 ppm, respectively. Then, the temperature dependence, $\Delta\delta/\Delta T$, of the amide proton chemical shift was analyzed. It is 1.7, 6.5, and 7.4 ppb/K for compounds **1c**, **1f**, and **1g**, respectively (see Table 1). These data reveal that the hydrogen bond of **1c** is strong ($\Delta\delta \leq 0.2$, $\Delta\delta/\Delta T < 3$) and those of **1f** and **1g** are weak or nonexistent ($\Delta\delta > 0.2$, $\Delta\delta/\Delta T > 3$).[46]

Hence, we can conclude that the thermal properties of these model systems can be modified by replacing the vinylic hydrogen by a methyl group and/or changing the aryl moiety.

Table 1. Hydrodynamic Volume (V_H), Volume Ratio, Amide Proton Chemical Shift Variation from $CDCl_3$ to DMSO-d^6 ($\Delta\delta$), and Its Temperature Dependence ($\Delta\delta/\Delta T$) for Compounds 1c,e–g

compd	V_H (Å^3)	vol ratio	$\Delta\delta$ (ppm)	$\Delta\delta/\Delta T$ (ppb/K)
1e	197.07	1		
1c	97.15	2.03	0.18	1.7
1f	88.14	2.24	1.30	6.5
1g	95.54	2.06	2.12	7.4

Photochemical Study. Once the thermal properties have been established, some photochemical properties were studied such as the maximum absorption wavelength (λ_{max}) and the photostationary state (PSS) (Table 2). First, the absorption spectrum for each compound was recorded (see Figure S1) and the effect of the aryl substitution and hydrogen bond interaction analyzed. For compounds **1b**,**c**,**e**,**f**–**i**, a red-shift of λ_{max} was observed, compared to **1a**, due to (i) introduction of an electron-donating group in the aryl moiety (e.g., OMe in **1h**,**j**), (ii) conjugation increase (e.g., a naphthyl ring in **1b**), (iii) five-membered ring aromaticity and electron confinement reduction (e.g., pyrrole, furan, or thiophene rings in **1e**,**f**,**g** compared to the phenyl ring, **1a**), and (iv) hydrogen bond interactions (e.g., **1c**,**e**). It is noteworthy that the shift observed for **1e** is surprisingly large, and it can be attributed not only to the larger electronic density of the ring, compared to the furan or thiophene rings, but also to its intermolecular hydrogen-bond interaction, as previously concluded.

Table 2. Maximum Absorption Wavelength (λ_{max}), Molar Absorptivity (ε), and Photostationary State (PSS) of Compounds 1a–j and 2a–c in $CHCl_3$

compd	λ_{max} (nm)	ε (M^{-1} cm^{-1})	PSS (*Z*/*E*)
***Z*-1a**	326	17200	57:43
***Z*-1b**	336	20000	68:32
***Z*-1c**	350	21500	100:0
***Z*-1d**	318	22000	57:43
***Z*-1e**	369	11000	90:10
***Z*-1f**	350	26000	80:20
***Z*-1g**	349	25000	70:30
***Z*-1h**	338	19900	67:33
***Z*-1i**	336	23300	62:38
***Z*-1j**	324	20500	55:45
***E*-2a**	295	22800	50:50
***E*-2b**	280	16500	50:50
***E*-2c**	292	15000	71:29
***Z*-2c**	344	34500	71:29

In order to further analyze the effect of the hydrogen-bond interaction on λ_{max}, we compared the values of ***Z*-1c** (2-Py) with ***Z*-1d** (4-Py) and ***E*-2c** with ***Z*-2c**. For ***Z*-1c** and ***Z*-2c**, a red-shift of 42 and 52 nm was observed due to their strong hydrogen-bond interaction compared to ***Z*-1d** and ***E*-2c**, respectively (see Figure 4).

Moreover, we have noticed that the absorption spectra of ***E*-1a** and ***E*-2a** are blue-shifted compared to their respective *Z*

DOI: 10.1021/acs.joc.6b00892
J. Org. Chem. 2016, 81, 6292–6302

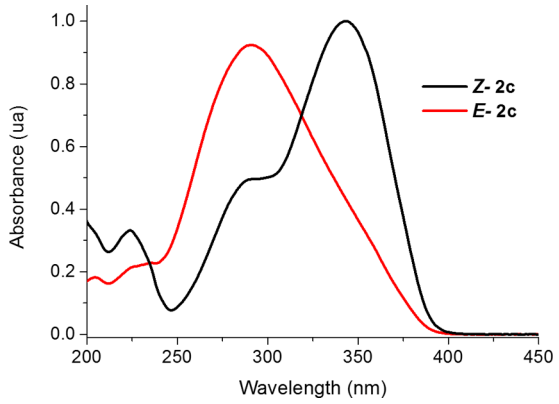

Figure 4. Normalized absorption spectra of *Z*-**2c** and *E*-**2c**.

isomers (see Figure 5). This difference can be explained in terms of electronic structure (see the Discussion).

After studying the absorption properties, all compounds were irradiated in a 400 W medium-pressure Hg lamp in a Pyrex NMR tube in order to measure their photostationary state (PSS). The photoisomerization was easily followed by ^{1}H NMR as the chemical shifts of certain protons of both isomers are different enough (see Figure S6). Irradiation was kept until the PSS was reached (Table 2). In this case, no significant variation due to the electronic nature of the substituent or the aryl moiety was observed (see compounds **1b,d,h-j,2b** in Table 2). Whereas, the hydrogen bond interaction, either intra- or intermolecular, influences the photoisomerization process (see compounds **1c,e-g,2c** in Table 2). For compound **1c** (2-Py), where a strong hydrogen bond is formed, the photoisomerization is completely blocked. Along this line, the PSS measured for **1e** (pyrrole), **1f** (furan), and **1g** (thiophene) is lower than expected, and the percentage of photoisomer, *E* isomer, increases from **1e** < **1f** < **1g** as the intramolecular hydrogen bond strength decreases in the same order (see Synthesis and Thermal Properties). Similarly, the PSS of **2c** is enriched in *Z* isomer as an intramolecular hydrogen bond interaction is possible but not strong enough to block the photoisomerization. Hence, we can conclude that the main feature affecting the photochemical properties (λ_{max} and PSS) is the hydrogen-bond interaction.

The direct dependence of the photoisomerization extent on the hydrogen bond strength can be also useful in order to control the photoisomerization process by means of different external inputs. With this aim, we selected compound *Z*-**1e**, whose intermolecular hydrogen-bond interactions are well established, and two different external inputs, light and acid (trifluoroacetic acid, TFA)/base (triethylamine, NEt_3), to build a cycle of four stages (see Figure 6).

In order to monitor the process, we first recorded the ^{1}H NMR spectrum of compound **Z-1e**, stage 1 in Figure 7. We then added 1 equiv of TFA and observed that the signals shifted to low fields, stage 2 in Figure 7. Once compound **Z-1e** is protonated, the intermolecular hydrogen bond interaction is disrupted and the system isomerizes after irradiation (PSS of 62/38 (*Z*/*E*)), stage 3 in Figure 7. Afterward, 1 equiv of NEt_3 was added to again deprotonate the molecule, without modifying the PSS, stage 4 in Figure 7. We observed how the signals were shifted to high fields and one pair was coincident with the ones of the parent compound. After irradiation, the PSS was reached (see Table 2), observing that it is enriched in the *Z* isomer (90%), stage 5 in Figure 7. This fact can be explained by intermolecular hydrogen bonds in the *Z* isomer that block the $Z \rightarrow E$ photoisomerization.

Photoisomerization Dynamics. In order to understand the dynamic processes that take place after photoexcitation of these model systems, we applied UV−vis transient absorption spectroscopy (see the Experimental Section for details). We selected compounds *Z*-**1a** and *E*-**2a** as the representative derivatives for each model family and $CHCl_3$ as solvent. By comparing the performance of these compounds, we could understand the effect of the critical structural modifications discussed above. The effect of the hydrogen bonding, while relevant for the photochemical properties as shown in the previous sections, would only affect the time scale of the excited-state decay (see below) and, thus, will not be considered here. The excitation wavelengths were chosen to be 340 nm for *Z*-**1a** and 300 nm for *E*-**2a** and thus slightly red-shifted with respect to the absorption maxima (see Table 2 and Figure 5) in order to reduce excess energy in the excited state. Additionally, experiments were performed at 340 nm for *E*-**2a** in order to compare the relaxation behavior of both compounds excited with the same energy. Figure 8 shows the transient absorption changes (ΔOD) mapped as a function of the probe wavelengths and pump−probe time delay, where positive ΔOD is coded in red.

Regarding compound *Z*-**1a**, a positive band centered at 490 nm was observed (see Figure 8A) that corresponds to the excited-state absorption (ESA). For compound *E*-**2a**, two positive absorption bands around 520 and 660 nm were observed (see Figure 8B,C). The transient absorption profiles pumped at 340 nm were globally fitted by a biexponential decay revealing two ultrafast time constants on the femtosecond (τ_1)

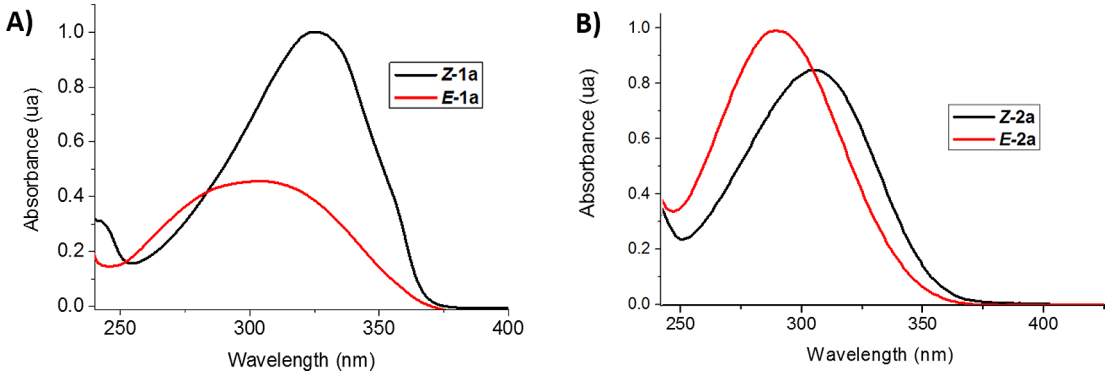

Figure 5. Normalized absorption spectra of compounds (A) **1a** and (B) **2a**.

DOI: 10.1021/acs.joc.6b00892
J. Org. Chem. 2016, 81, 6292−6302

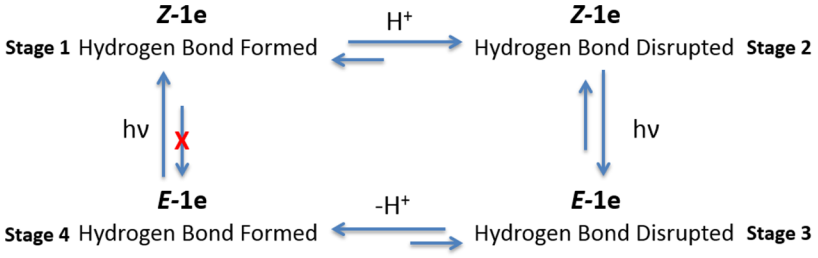

Figure 6. Four-stages cycle for compound **1e** using two different external inputs.

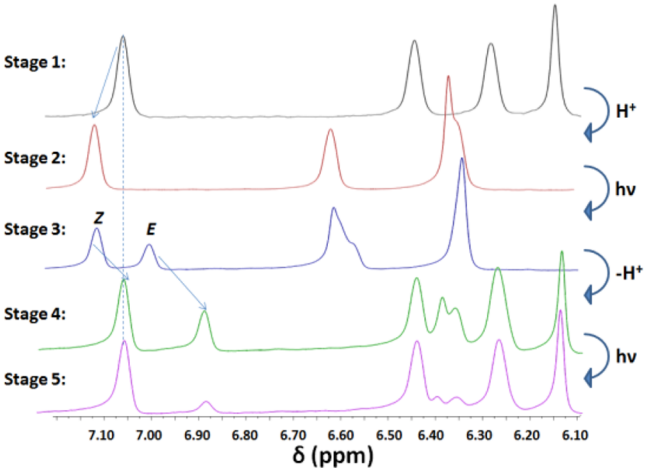

Figure 7. ^{1}H NMR signals in the aromatic region for the four stages needed to complete the cycle.

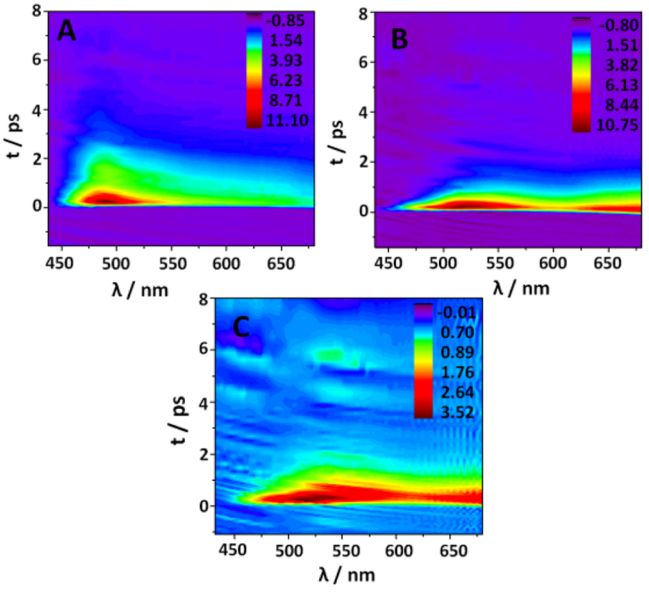

Figure 8. Transient absorption changes (ΔmOD) as a function of the probe wavelength and pump−probe time delay pumped at 340 nm of (A) ***Z*-1a**, (B) ***E*-2a**, and (C) ***E*-2a** pumped at 300 nm.

and (sub-) picosecond (τ_2) time scale. The results are quite similar for compound ***Z*-1a** and ***E*-2a**. In contrast, the transient absorption profile of ***E*-2a** pumped at 300 nm was modeled by a monoexponential decay (τ_2). All time constants are listed in Table 3. However, as τ_1 is close to the experimental time resolution, the corresponding decay could also be faster than the values may suggest.

Table 3. Time Constants Obtained from Global Fits of Each Transient Absorption Spectrum for Compounds 1a and 2a

compd	λ_{pump} (nm)	τ_1 (ps)	τ_2 (ps)
1a	340	0.18	1.87
2a	340	0.26	0.97
2a	300		0.61

Concerning Figure 5, the photochemical isomers which are built after excitation reveal absorption bands in the ultraviolet region. Since the sapphire-generated white light is limited to 435 nm, single-color probe experiments were additionally performed in the UV to check for complete ground-state recovery. The corresponding transients of Figure 9 show photoproduct absorption (PA) as well as ground-state bleaching (GSB) of the photochemical and the most thermally stable isomers for compound ***Z*-1a** pumped at 340 nm and compound ***E*-2a** pumped at 300 nm, respectively.

Regarding compound ***Z*-1a**, 345 and 330 nm were selected as the probe wavelengths. Their transient absorption profiles are quite similar (see Figure 9A). An intense negative signal is observed mainly due to the GSB of the thermally stable isomer. At 330 nm, a positive band is observed around time zero indicating ESA that dominates the visible spectral part (see Figure 9A). However, in the UV part, ESA is superimposed by GSB, which dominates in this regime and can be attributed to pure ground-state recovery. At 345 nm, the early-time ESA is not seen, most likely due to chirp under nonoptimized dispersion compensation conditions. The slightly different recovery profiles at 330 and 345 nm on a picosecond time scale may arise from absorption of hot vibrational photoproduct or reactant (HGSA). This superposition is much more obvious for ***E*-2a** (see below). At longer times, the transients do not fully recover, indicating slower processes and/or incomplete switching. This is in line with Figure 5, demonstrating that the *E* and *Z* isomers show significant absorptive overlap which cannot be completely separated by photoexcitation.

Compound ***E*-2a** was pumped at 300 nm and probed at 345, 330, and 305 nm; see Figure 9B. As a consequence of the observed superposition of excited-state absorption and ground-state bleaching in the UV region, these transient absorption profiles cannot be described by simple exponential kinetics. A detailed discussion on how the individual components would be appropriately treated is given by earlier studies of Briand and Temps et al.[47−50] In our case, such a thorough analysis is not possible because the important spectral window between 345 and 430 nm where most likely hot ground-state absorption prevails is lacking. On the other hand, a detailed analysis of these data is well beyond the scope of this paper.

Computational Study. Finally, a computational study of compounds **1a**, **1c**, **1f**, and **2a** has been performed. The different *Z*/*E* relative stabilities and excited-state lifetimes of **1a**

DOI: 10.1021/acs.joc.6b00892
J. Org. Chem. 2016, 81, 6292−6302

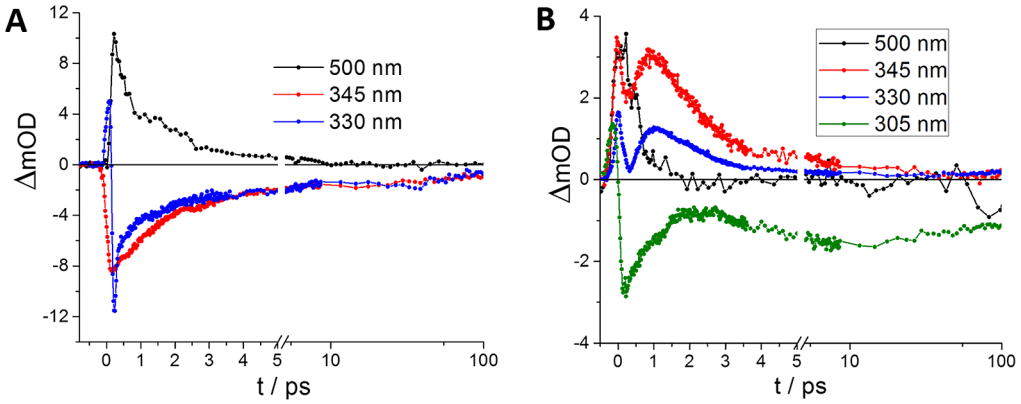

Figure 9. Transient absorption profiles at selected probe wavelengths for (A) compound ***Z*-1a**, pumping at 340 nm, and (B) compound ***E*-2a**, pumping at 300 nm.

and **2a** and, moreover, the effect of hydrogen bonding on the excited state compared to the MEPs of **1a**, **1c**, and **1f** have been analyzed. Regarding the different thermal behavior of **1a** and **2a**, first the ground-state minima of ***Z*-1a**, ***E*-1a**, ***Z*-2a**, and ***E*-2a** were optimized at the MP2/6-31g(d) level of theory, taking into account the solvent effect (see Computational Details).

Concerning the thermal stability, it was found that ***Z*-1a** is 3.5 kcal·mol^{-1} more stable than ***E*-1a**, whereas ***E*-2a** is around 1 kcal·mol^{-1} more stable than ***Z*-2a**. The inversion of the relative thermal stability for compound **2a** can be explained by the steric hindrance between the two methyl groups in ***Z*-2a** (Figure 10C), which is relieved in ***E*-2a** (Figure 10D) by

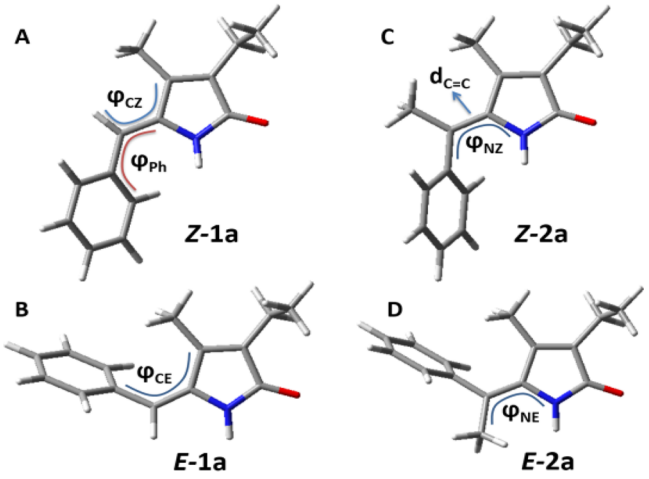

Figure 10. Ground-state minima structures of (A) ***Z*-1a**, (B) ***E*-1a**, (C) ***Z*-2a**, and (D) ***E*-2a**. φ_{CZ}, φ_{CE}, φ_{NZ}, φ_{NE}, φ_{Ph}, and $d_{C=C}$ are depicted.

rotation of the phenyl ring (ca. 60°). For compound **1a**, the *Z* isomer is the most thermally stable due to its more planar and conjugated structure compared to ***E*-1a** ($\varphi_{CZ(CE)}$ = −4.5 (12.6)°; φ_{Ph} = 37 (57)° for ***Z*-1a** (***E*-1a**)). Moreover, analyzing the values of φ_{CE}, φ_{CZ}, and $d_{C=C}$ (Table 4), it is observed that the carbon−carbon double-bond distance is slightly longer for **2a**, compared to **1a**, and that the torsion around this bond is more advanced for the *E* isomers.

The absorption spectra and minimum energy paths of these two compounds were then calculated to understand the different excited-state dynamics experimentally found by TAS. First, the absorption spectra of ***Z*-1a**, ***E*-1a**, ***Z*-2a**, and ***E*-2a** were simulated at the TD-DFT/6-31g(d) level of theory, taking into

Table 4. Structural Parameters (φ_{CZ}, φ_{CE}, φ_{NZ}, φ_{NE}, and $d_{C=C}$) for the Ground-State Minima of Compounds *Z*-1a, *E*-1a, *Z*-2a, and *E*-2a Calculated at the MP2/6-31g(d) Level of theory

compd	$d_{C=C}$ (Å)	φ_{CZ}, φ_{CE} (deg)	φ_{NZ}, φ_{NE} (deg)
***Z*-1a**	1.357	−4.5	−1.5
***E*-1a**	1.357	12.6	5.2
***Z*-2a**	1.364	−3.3	−5.8
***E*-2a**	1.362	15.0	3.3

account the solvent effect (see the Computational Details). For all of the compounds, the optical bright state is the first singlet excited state, S_1, whose electronic transition is mainly described by the excitation of one electron from the bonding, π, to the antibonding, π^*, orbital of the central carbon−carbon double bond (see Figure S7). This means that after excitation the photoisomerizable formal double bond is elongated, allowing rotation around this bond. The calculated excitation energies (in nm) were 348 (317) and 310 (284) for compounds ***Z*-1a** (***E*-1a**) and ***Z*-2a** (***E*-2a**), respectively (Table S3), in very good agreement with the absolute experimental values as well as the blue/red-shift experimentally observed.

Furthermore, the minimum energy paths (MEPs) of compounds ***Z*-1a** and ***E*-2a** were computed. From the Franck−Condon (FC) geometry, both ***Z*-1a** and ***E*-2a** minimize the energy in S_1 along the stretching coordinate. The formal carbon−carbon double bond is elongated, resulting in a bond length alternation of single and double bonds, as predicted by the electronic nature of the vertical transition. Once the stretching mode is relaxed, the system starts to rotate around the photoisomerizable central carbon−carbon double bond until it reaches a conical intersection (CI) with the ground state at ca. 90° of rotation (see Figure 11). From here, the system may decay to the ground state, completing the photoisomerization or reverting to the initial isomer. Analyzing the data in Figure 11, we observe that the minimum energy path along the torsion coordinate, (φ_{NZ} or φ_{NE}) for ***Z*-1a** is very flat, whereas for compound ***E*-2a** the path is much steeper and the excess vibrational energy from the FC to the CI is ca. 14 kcal·mol^{-1} higher, which could accelerate the motion toward the CI.

Finally, the minimum energy paths of ***Z*-1c** and ***Z*-1f** have been computed and compared with the one of ***Z*-1a** (see Figure 11 and Figure S9). As previously shown (see Synthesis and Thermal Properties), a hydrogen-bond interaction is present in compounds ***Z*-1c** (Ar = 2-pyridine) and ***Z*-1f** (Ar = 2-furan)

DOI: 10.1021/acs.joc.6b00892
J. Org. Chem. 2016, 81, 6292−6302

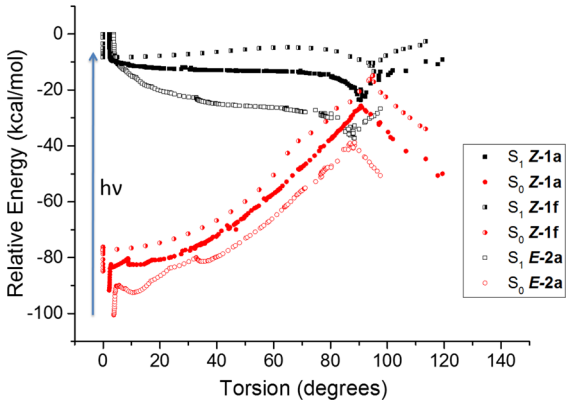

Figure 11. Minimum energy paths of ***Z*-1a**, ***Z*-1f**, and ***E*-2a** along the torsion coordinate (φ_{NZ} and φ_{NE}, respectively) in S_1 from the FC structure.

that is strong enough to block the photoisomerization process for **1c**. By analyzing their MEPs, we can observe that after excitation to the bright state the system first activates the stretching mode, similarly to ***Z*-1a**. Then, a minimum in S_1 has been found for both ***Z*-1c** and ***Z*-1d**, due to the hydrogen-bond interaction that hampers the rotation around the photoisomerizable double bond. From here, the system has to overcome an energy barrier along the torsion coordinate up to reaching the S_1/S_0 conical intersection. The energy barriers computed were 3.5 and 4.6 kcal/mol for ***Z*-1f** and ***Z*-1c**, in line with the stronger hydrogen-bond interaction experimentally measured for ***Z*-1c** (see Figure S9). Hence, it can be concluded that the presence of a hydrogen-bond interaction clearly influences the excited state, increasing the energy barrier along the torsion coordinate which value is directly related to the hydrogen bond strength. For the same reason, it can be stated that the excited-state lifetime will be increased with the hydrogen-bond strength.

DISCUSSION

First, the rationalization of the structural effects that control the *Z*/*E* relative thermal stability is a key point to facilitate the isolation and characterization of the photoproduct and, even more relevant, to decrease the dark reversion rate, as discussed in the Introduction. With this purpose, we analyzed three cases: (i) compound **1a**, whose thermally stable isomer is the *Z* isomer; (ii) compound **2a**, for which the *Z*/*E* relative stability is reverted and the *E* isomer is the most thermally stable, and (iii) compound **2c**, an intermediate situation where the energy of both isomers is similar. To understand these differences, we can argue in terms of steric hindrance, conjugation extent, and hydrogen-bond interactions. Regarding compound **1a**, the *Z* isomer is the most thermally stable due to its more planar and, hence, more conjugated structure, compared to ***E*-1a**, as suggested by the structural parameters of the ground-state minima computed (Table 4), whereas for **2a** the main effect responsible for the *Z*/*E* relative stability inversion is the steric hindrance between the two methyl groups in the *Z* isomer, destabilizing it (see Figure 10C). Moreover, the similar thermal stability found for ***E*-2c** and ***Z*-2c** can be easily explained: the *Z* isomer is destabilized by steric hindrance between the two methyl groups of the structure but stabilized by intramolecular hydrogen-bond interaction ($\delta_{\text{amide proton}}$= 11.44 ppm, see the Supporting Information). On the other hand, the *E* isomer is of comparable stability as the steric hindrance is released by rotation of the phenyl ring (see Figure 3). Hence, we may control the thermal carbon−carbon double bond configuration by means of minor structural changes.

In addition, the establishment of hydrogen-bond interactions is a crucial feature in bilirubin and bilin pigments. They do influence not only the thermal properties but also the photochemical ones such as the absorption spectrum or the photoisomerization process. For instance, a significant red-shift of the absorption spectrum is observed for the isomer with hydrogen bonds which, in turn, increases the separation between the absorption bands of both isomers (Figure 5). We can take advantage of this evidence and guide the design of derivatives with long absorption wavelength, desirable for biological applications, and large absorption difference of both isomers, increasing the irradiation selectivity. On the other hand, we have confirmed that the strength of the hydrogen bond has a direct effect on the photoisomerization extent, more in particular on the PSS. The percentage of the initial isomer in the PSS can be modulated by the hydrogen-bond strength, even blocking the photoisomerization process as observed for compound **1c** (Table 2).

Finally, we can give insight into the first steps and the photoisomerization mechanism of these model systems by a combined experimental TAS and theoretical analysis. Considering the transient absorption spectra pumped at 340 nm (Figure 8A,B), two time constants were obtained characterizing the excited-state dynamics of ***Z*-1a** and ***E*-2a** (Table 3). Analyzing the MEPs computed for our models, the first time constant, τ_1, is attributable to the activation of the stretching mode, high frequency mode, which elongates the central carbon−carbon double bond from the FC region (see Figure 11 and Figure S8). This process takes place within a few hundred femtoseconds. Compared to the literature, such an ultrafast component was also observed in phytochrome.[51] As observed in the MEPs (Figure 11), once the stretching motions are completed, the system minimizes the energy along the torsional mode (low frequency mode), rotating around the former carbon−carbon double bond upon reaching a conical intersection with the ground state. This relaxation pathway is associated with the second time constant, τ_2, on a (sub)-picosecond time scale (see Figure 12).

Moreover, no intermediates such as minima in the excited state were found along the MEP. This evidence is in line with the time scale of τ_2, as it is generally larger when intermediates are present in the process (e.g., in phytochrome the first

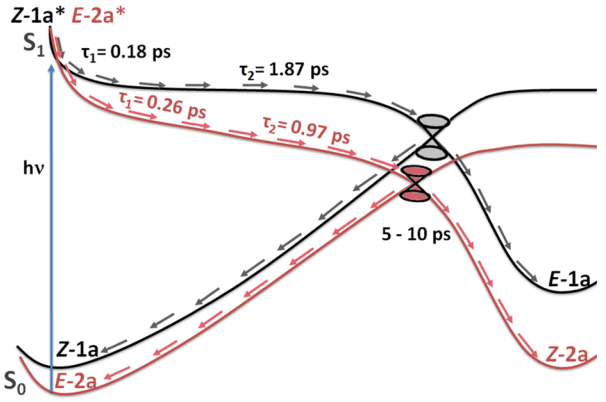

Figure 12. Schematic representation of the photoisomerization process for compounds ***Z*-1a** and ***E*-2a**.

DOI: 10.1021/acs.joc.6b00892
J. Org. Chem. 2016, 81, 6292−6302

isomerized excited state intermediate is formed in 3 ps, as there is a local minimum due to a interaction of a ring with the protein).[51] However, the excited-state decay of these models is longer lived than the ones found for downhill processes such the photoisomerization of the retinal protonated Schiff base in rhodopsin (~200 fs).[52] This fact can be due to the flat profile along the torsion coordinate in the MEP that slows the process.

Additionally, we can compare the photodynamics of compounds ***Z*-1a** and ***E*-2a**. We observed that the excited state decay, τ_2, is almost two times faster for ***E*-2a** when pumping at 340 nm. This fact is in agreement with the steeper path along the torsion coordinate computed for ***E*-2a**. The different potential energy surface topologies can be rationalized in terms of structural parameters related to the photoisomerization process. Along this line, we can analyze the central carbon−carbon double-bond distance ($d_{C=C}$) and its pretwist (φ_{CZ}, φ_{CE}). Concerning $d_{C=C}$, it is slightly larger for ***E*-2a** (Table 4) compared to ***Z*-1a** in the ground-state minima, and this trend is kept along the MEP (see Figure S4). This implies a higher character of single bond of the photoisomerizable double bond for ***E*-2a** which could favor the rotation around this bond. Another important structural parameter that could influence the photochemistry is the pretwist of the photoisomerizable double bond. The pretwist of ***E*-2a** (φ_{CE} = 15.0°) is larger than the one of ***Z*-1a** (φ_{CZ} = −4.5°). This increases the initial velocity out of the FC region along the torsion coordinate for ***E*-2a**, finding a steepest profile. Thus, the electronic and steric effects of the methyl group in the vinylic position modify both the relative stability of *Z*/*E* isomers and their photochemistry.

Considering the transient absorption spectrum of ***E*-2a** pumped at 300 nm (Figure 8C), monoexponential decay of ΔmOD was observed within 0.61 ps (τ_2, Table 3). In contrast to the experiments performed at 340 nm, excitation at 300 nm leads to higher excess energy in the initially excited state. Thus, it is plausible that the activation of the stretching mode is within our experimental time resolution. The obtained time constant, τ_2, is associated with the excited-state dynamics toward a conical intersection with the ground state.

Finally, we have analyzed the effect of the hydrogen-bond interaction in the excited state by comparing the MEPs of ***Z*-1a**, ***Z*-1c**, and ***Z*-1f**. It has been demonstrated that a minimum in S_1 appears for **1c** and **1f** as a consequence of the hydrogen-bond interaction. Moreover, the system has to overcome an energy barrier along the torsion coordinate proportional to the hydrogen-bond strength. Hence, the stronger is the interaction the higher is the energy barrier, increasing the excited state lifetime and even, blocking the photoisomerization process as is the case of ***Z*-1c**.

CONCLUSION

In this work, we have presented a combined experimental (synthesis and characterization) and theoretical study of two different families of bilin chromophores and bilirubin model systems. First, we have been able to control the *Z*/*E* relative thermal stability by minor structural changes. Thanks to the analysis of the structural parameters and the NMR data, we have concluded that the steric hindrance, conjugation extent and hydrogen bond interactions are the principal factors that govern this property. In addition, we have confirmed that hydrogen bond interactions influence also the photochemical properties, red-shifting the absorption spectrum, or modifying the PSS and the MEP according to the hydrogen bond strength. Hence, the design of derivatives with hydrogen bonds could be used to stabilize to a large extent one of the isomers and red-shift the λ_{max} but it can also decrease the photoisomerization efficiency.

In addition, the excited-state dynamics of ***Z*-1a** and ***E*-2a** have been studied by TAS and the MEPs of ***Z*-1a**, ***Z*-1c**, ***Z*-1f**, and ***E*-2a** computed along S_1. Regarding ***Z*-1a** and ***E*-2a**, a fast relaxation out of the FC region due to stretching motions was observed, τ_1, followed by a barrierless rotation around the former central double bond, in agreement with the time scale of τ_2. Moreover, we observed that the excited-state decay of ***E*-2a** is sped up regarding to ***Z*-1a**, due mainly to their different electronic structure ($d_{C=C}$ and pretwist). Finally, it has been shown that the hydrogen-bond interaction has a clear influence on the MEP, appearing as an energy barrier along the torsion coordinate whose value depends on the interaction strength.

In summary, this study can guide the design of both structurally modified phytochrome chromophores and novel protein mutants.[53,54] This may be relevant for the tuning of the properties of phytochromes and also to generate novel chromoproteins with different functions. Moreover, this work can help to better understand the photodynamics of the chromophores in vivo.

EXPERIMENTAL SECTION

General Information. ^{1}H and ^{13}C NMR spectra were recorded on a 400 MHz NMR spectrometer. Signal patterns are depicted as s (singlet), d (doublet), t (triplet), q (quartet), and m (multiplet). Electrospray mass spectra were recorded on a mass spectrometer using the ESI mode. For the photostationary state measurement, a solution of the sample was placed in a Pyrex NMR tube and irradiated in a 400 W medium-pressure mercury lamp, and the photoproduct formation was quantified by NMR. X-ray data were collected with an area-detector diffractometer using graphite-monochromatic Mo Kα irradiation. Images were processed using the DENZO and SCALEPACK suite of programs.[55]

Time-Resolved Experimental Methods. The ultrafast dynamics of the synthesized compounds **1a** and **2a** were studied by femtosecond transient absorption spectroscopy. Pulses of 150 fs duration with 1.6 mJ/pulse at a repetition rate of 1 kHz and a central wavelength of 775 nm were generated by a CPA 2210 laser system.[56] The experimental setup employed for transient absorption spectroscopy is described in more detail elsewhere.[57] The pump wavelengths of 300 and 340 nm were generated by frequency doubling. For probing, a sapphire generated white light in the spectral range from 435 to 680 nm. The experimental setup employed for single-color probe measurements is described in more detail elsewhere.[58] The pump wavelengths of 300 and 340 nm were generated by sum frequency mixing.[59] The probe wavelength of 500 nm was generated by a noncollinearly optical parametric amplifier (NOPA) system.[60] Additionally, probe wavelengths of 305, 330, and 345 nm were generated by frequency doubling of the visible NOPA output. All measurements were carried out under magic angle (54.7°) conditions at room temperature and an optical density of 2.5 in order to minimize the group velocity mismatch of pump and probe beam. Moreover, to avoid the local buildup of photoproducts, the sample was continuously pumped through a fused silica cuvette with 1 mm optical path length. Data acquisition was performed using in house software in a Labview environment resulting in pump-induced, time-resolved changes of the optical density (ΔOD). For details, see ref 57. The error is estimated to be 0.2 ps for τ1 and 0.1 ps for τ2.

Computational Details. Ground-state minima were optimized at the MP2/6-31g(d) level of theory taking into account the solvent effect by means of the polarizable continuum model (PCM).[61] The absorption spectra and the minimum energy paths on the excited state were simulated at the TD-DFT/6-31g(d) level of theory with the CAM-B3LYP[62] hybrid functional, taking into consideration the solvent

DOI: 10.1021/acs.joc.6b00892
J. Org. Chem. 2016, 81, 6292−6302

effect with the PCM model. All calculations were performed with Gaussian 09 software.[63]

Synthesis of Compounds 1a–j and 2a–c. In a round-bottom flask were dissolved 1 mmol of the desired carbonyl compound and 2 mmol (0.250 g) of 3-ethyl-4-methyl-1*H*-pyrrol-2(5*H*)-one in 5 mL of DMSO. Once those compounds were dissolved, 1.5 mL of KOH 4 M was added. The mixture was stirred under argon at 60 °C for 12 h. The reaction mixture was poured into 20 mL of water, and the precipitate obtained was collected by vacuum filtration and washed with cold water.

*(Z)-5-Benzylidene-3-ethyl-4-methyl-1H-pyrrol-2(5H)-one (**Z-1a**).* Yield = 81% (0.1726 g, mp 136–137 °C). ^{1}H NMR (400 MHz, $CDCl_3$): δ 7.89 (s, 1H), 7.43 (d, J = 4.4 Hz, 4H), 7.35–7.30 (m, 1H), 6.13 (s, 1H), 2.43 (q, J = 7.6 Hz, 2H), 2.16 (s, 3H), 1.17 (t, J = 7.6 Hz, 3H). ^{13}C NMR (400 MHz, $CDCl_3$): δ 172.7 (s), 141.2 (s), 138.1 (s), 135.2 (s), 133.9 (s), 129.1 (s), 128.5 (s), 127.7 (s), 108.0 (s), 16.9 (s), 13.3 (s), 9.7 (s). UV–vis ($CHCl_3$): λ(nm) = 196 (ε = 25500 M^{-1} cm^{-1}), 228 (ε = 6800 M^{-1} cm^{-1}), 326 (ε = 17200 M^{-1} cm^{-1}). EM-ES(+): ($C_{14}H_{15}NO$ + H) calcd 214.1232, found 214.1233. Observations: yellow solid.

*(E)-5-Benzylidene-3-ethyl-4-methyl-1H-pyrrol-2(5H)-one (**E-1a**).* ^{1}H NMR (400 MHz, $CDCl_3$) δ 9.07 (s, 1H), 7.24–7.36 (m, 5H), 6.62 (s, 1H), 2.35 (q, J = 7.3 Hz, 1H), 1.73 (s, 1H), 1.09 (t, J = 7.5 Hz, 1H). ^{13}C NMR (400 MHz, $CDCl_3$): δ 172.0 (s), 139.0 (s), 139.0 (s), 138.2 (s), 135.2 (s), 129.7 (s), 128.1 (s), 127.6 (s), 113.9 (s), 16.7 (s), 13.3 (s), 13.2 (s). UV–vis ($CHCl_3$): λ(nm) 304 (ε = 13800 M^{-1} cm^{-1}). EM-ES(+): ($C_{14}H_{15}NO$ + H) calcd 214.1232, found 214.1233.

*(Z)-3-Ethyl-4-methyl-5-((naphthalen-2-yl)methylene)-1H-pyrrol-2(5H)-one (**Z-1b**).* Yield = 88% (0.2316 g, mp 191–192 °C). ^{1}H NMR (400 MHz, $CDCl_3$): δ 8.14 (s, 1H), 7.92 (s, 1H), 7.89–7.80 (m, 3H), 7.54–7.44 (m, 3H), 6.24 (s, 1H), 2.42 (q, J = 7.6 Hz, 2H), 2.16 (s, 3H), 1.15 (t, J = 7.6 Hz, 3H). ^{13}C NMR (400 MHz, $CDCl_3$): δ 172.9 (s), 141.4 (s), 138.4 (s), 133.9 (s), 133.7 (s), 132.7 (s), 132.6 (s), 128.8 (s), 128.2 (s), 127.7 (s), 127.6 (s), 126.7 (s), 126.5 (s), 126.4 (s), 108.2 (s), 16.9 (s), 13.4 (s), 9.7 (s). UV–vis ($CHCl_3$): λ(nm) = 213 (ε = 33400 M^{-1} cm^{-1}), 279 (ε = 21400 M^{-1} cm^{-1}), 336 (ε = 20000 M^{-1} cm^{-1}). EM-ES(+): ($C_{18}H_{17}NO$ + H) calcd 264.1388, found 264.1387. Observations: yellow solid.

*(Z)-3-Ethyl-4-methyl-5-((pyridin-2-yl)methylene)-1H-pyrrol-2(5H)-one (**Z-1c**).* Yield = 94% (0.2013 g). ^{1}H NMR (400 MHz, $CDCl_3$): δ 10.48 (s, 1H), 8.57 (d, J = 4.7 Hz, 1H), 7.66 (t, J = 7.7 Hz, 1H), 7.25 (d, J = 7.9 Hz, 1H), 7.14–7.07 (m, 1H), 5.93 (s, 1H), 2.43 (q, J = 7.6 Hz, 2H), 2.12 (s, 3H), 1.16 (t, J = 7.6 Hz, 3H). ^{13}C NMR (400 MHz, $CDCl_3$): δ 172.2 (s), 155.8 (s), 149.2 (s), 142.8 (s), 140.0 (s), 136.6 (s), 135.2 (s), 124.6 (s), 121.0 (s), 103.5 (s), 16.9 (s), 13.4 (s), 9.4 (s). UV–vis ($CHCl_3$): λ(nm) = 192 (ε = 34300 M^{-1} cm^{-1}), 279 (ε = 5600 M^{-1} cm^{-1}), 350 (ε = 21500 M^{-1} cm^{-1}). EM-ES(+): ($C_{13}H_{14}N2O$ + H) calcd 215.1184, found 215.1212. Observations: yellow solid.

*(Z)-3-Ethyl-4-methyl-5-((pyridin-4-yl)methylene)-1H-pyrrol-2(5H)-one (**Z-1d**).* Yield = 76% (0.1627 g, mp 144–145 °C). ^{1}H NMR (400 MHz, $CDCl_3$): δ 8.82 (s, 1H), 8.63 (d, J = 5.0 Hz, 2H), 7.36 (d, J = 5.3 Hz, 2H), 5.99 (s, 1H), 2.43 (q, J = 7.5 Hz, 2H), 2.15 (s, 3H), 1.17 (t, J = 7.6 Hz, 3H). ^{13}C NMR (400 MHz, $CDCl_3$): δ 173.2 (s), 150.4 (s), 142.6 (s), 141.3 (s), 141.2 (s), 135.2 (s), 122.9 (s), 104.9 (s), 17.0 (s), 13.2 (s), 9.7 (s). UV–vis ($CHCl_3$): λ(nm) = 197 (ε = 9500 M^{-1} cm^{-1}), 223 (ε = 5100 M^{-1} cm^{-1}), 318 (ε = 22000 M^{-1} cm^{-1}). EM-ES(+): ($C_{13}H_{14}N_2O$ + H) calcd 215.1184, found 215.1188. Observations: yellow solid.

*(Z)-5-((1H-Pyrrol-2-yl)methylene)-3-ethyl-4-methyl-1H-pyrrol-2(5H)-one (**Z-1e**).* Yield = 80% (0.1617 g, mp: 110–111 °C). ^{1}H NMR (400 MHz, $CDCl_3$): δ 11.09 (s, 1H), 10.77 (s, 1H), 7.05 (s, 1H), 6.45 (s, 1H), 6.28 (s, 1H), 6.17 (s, 1H), 2.44 (q, J = 7.5 Hz, 2H), 2.13 (s, 3H), 1.18 (t, J = 7.5 Hz, 3H). ^{13}C NMR (400 MHz, $CDCl_3$): δ 174.1 (s), 142.1 (s), 130.8 (s), 130.7 (s), 127.5 (s), 123.3 (s), 115.9 (s), 109.9 (s), 103.3 (s), 17.0 (s), 13.4 (s), 9.7 (s). UV–vis ($CHCl_3$): λ(nm) = 199 (ε = 9500 M^{-1} cm^{-1}), 265 (ε = 5700 M^{-1} cm^{-1}), 364 (ε = 11000 M^{-1} cm^{-1}). EM-ES(+): ($C_{12}H_{14}N_2O$ + H) calcd 203.1184, found 203.1184. Observations: green brown solid.

*(Z)-3-Ethyl-5-((furan-2-yl)methylene)-4-methyl-1H-pyrrol-2(5H)-one (**Z-1f**).* Yield = 80% (0.1625 g, mp: 97–98 °C). ^{1}H NMR (400 MHz, $CDCl_3$): δ 8.26 (s, 1H), 7.45 (s, 1H), 6.45–6.44 (m, 1H), 6.40 (d, J = 3.4 Hz, 1H), 5.85 (s, 1H), 2.37 (q, J = 7.6 Hz, 2H), 2.05 (s, 3H), 1.11 (t, J = 7.6 Hz, 3H). ^{13}C NMR (400 MHz, $CDCl_3$): δ 171.6 (s), 151.9 (s), 143.2 (s), 139.9 (s), 136.0 (s), 133.8 (s), 112.1 (s), 111.3 (s), 95.3 (s), 16.9 (s), 13.4 (s), 9.5 (s). UV–vis ($CHCl_3$): λ(nm) = 220 (ε = 6300 M^{-1} cm^{-1}), 283 (ε = 11000 M^{-1} cm^{-1}), 343 (ε = 26000 M^{-1} cm^{-1}). EM-ES(+): ($C_{12}H_{13}NO_2$ + H) calcd 204.1024, found 204.1028. Observations: dark reddish solid.

*(Z)-3-Ethyl-4-methyl-5-((thiophene-2-yl)methylene)-1H-pyrrol-2(5H)-one (**Z-1g**).* Yield = 98% (0.2147 g). ^{1}H NMR (400 MHz, $CDCl_3$): δ 7.57 (s, 1H), 7.37 (d, J = 5.0 Hz, 1H), 7.12 (d, J = 3.4 Hz, 1H), 7.08 (t, J = 4.2 Hz, 1H), 6.27 (s, 1H), 2.39 (q, J = 7.6 Hz, 2H), 2.10 (s, 3H), 1.13 (t, J = 7.6 Hz, 3H). ^{13}C NMR (400 MHz, $CDCl_3$): δ 171.8 (s), 141.1 (s), 138.3 (s), 136.3 (s), 133.9 (s), 128.1 (s), 127.9 (s), 126.4 (s), 101.1 (s), 17.0 (s), 13.3 (s), 9.6 (s). UV–vis ($CHCl_3$): λ(nm) = 202 (ε = 14700 M^{-1} cm^{-1}), 234 (ε = 4800 M^{-1} cm^{-1}), 350 (ε = 25000 M^{-1} cm^{-1}). EM-ES(+): ($C_{12}H_{13}NOS$ + H) calcd 220.0796, found 220.0787. Observations: yellow solid.

*(Z)-5-(4-Methoxybenzylidene)-3-ethyl-4-methyl-1H-pyrrol-2(5H)-one (**Z-1h**).* Yield = 83% (0.2018 g, mp 107–108 °C). ^{1}H NMR (400 MHz, $CDCl_3$): δ 7.69 (s, 1H), 7.33 (d, J = 8.6 Hz, 2H), 6.93 (d, J = 8.6 Hz, 2H), 6.04 (d, J = 6.6 Hz, 1H), 3.84 (s, 3H), 2.39 (q, J = 7.6 Hz, 2H), 2.11 (s, 3H), 1.13 (t, J = 7.6 Hz, 3H). ^{13}C NMR (400 MHz, $CDCl_3$): δ 172.7 (s), 159.2 (s), 141.3 (s), 136.7 (s), 133.3 (s), 129.9 (s), 127.8 (s), 114.7 (s), 108.0 (s), 55.4 (s), 16.9 (s), 13.4 (s), 9.7 (s). UV–vis ($CHCl_3$): λ(nm) = 191 (ε = 29700 M^{-1} cm^{-1}), 240 (ε = 9200 M^{-1} cm^{-1}), 338 (ε = 19900 M^{-1} cm^{-1}). EM-ES(+): ($C_{15}H_{17}NO_2$ + H) calcd 244.1337, found 244.1344. Observations: yellow solid.

*(Z)-5-(2-Methoxybenzylidene)-3-ethyl-4-methyl-1H-pyrrol-2(5H)-one (**Z-1i**).* Yield = 89% (0.2164 g, mp 147–148 °C). ^{1}H NMR (400 MHz, $CDCl_3$): δ 7.85 (s, 1H), 7.39 (d, J = 7.6 Hz, 1H), 7.30 (t, J = 7.8 Hz, 1H), 7.01 (t, J = 7.5 Hz, 1H), 6.95 (d, J = 8.3 Hz, 1H), 6.26 (s, 1H), 3.90 (s, 3H), 2.41 (q, J = 7.5 Hz, 2H), 2.16 (s, 3H), 1.15 (t, J = 7.6 Hz, 3H). ^{13}C NMR (400 MHz, $CDCl_3$): δ 172.2 (s), 156.8 (s), 141.2 (s), 138.0 (s), 133.9 (s), 129.9 (s), 129.3 (s), 124.2 (s), 121.2 (s), 111.3 (s), 103.9 (s), 55.7 (s), 16.9 (s), 13.3 (s), 9.7 (s). UV–vis ($CHCl_3$): λ(nm) = 203 (ε = 34800 M^{-1} cm^{-1}), 336 (ε = 23300 M^{-1} cm^{-1}).EM-ES(+): ($C_{15}H_{17}NO_2$ + H) calcd 244.1337, found 244.1334. Observations: yellow solid.

*(Z)-5-(4-Bromobenzylidene)-3-ethyl-4-methyl-1H-pyrrol-2(5H)-one (**Z-1j**).* Yield = 94% (0.2736 g, mp 146–147 °C). ^{1}H NMR (400 MHz, $CDCl_3$): δ 8.38 (s, 1H), 7.51 (d, J = 8.4 Hz, 2H), 7.30 (d, J = 8.4 Hz, 2H), 6.00 (s, 1H), 2.38 (q, J = 7.5 Hz, 2H), 2.11 (s, 3H), 1.13 (t, J = 7.5 Hz, 3H). ^{13}C NMR (400 MHz, $CDCl_3$): δ 173.3 (s), 141.3 (s), 138.5 (s), 134.0 (s), 132.1 (s), 130.3 (s), 121.6 (s), 107.1 (s), 17.0 (s), 13.3 (s), 9.7 (s). UV–vis ($CHCl_3$): λ(nm) = 194 (ε = 26200 M^{-1} cm^{-1}), 233 (ε = 9800 M^{-1} cm^{-1}), 324 (ε = 20500 M^{-1} cm^{-1}). EM-ES(+): ($C_{14}H_{14}BrNO$ + H) calcd 292.0337, found 292.0332. Observations: yellow solid.

*(E)-3-Ethyl-4-methyl-5-(1-phenylethylidene)-1H-pyrrol-2(5H)-one (**E-2a**).* Yield = 67% (0.1528 g, mp 200–201 °C). ^{1}H NMR (400 MHz, $CDCl_3$): δ 8.99 (s, 1H), 7.34 (t, J = 6.7 Hz, 3H), 7.22 (d, J = 7.7 Hz, 2H), 2.34–2.22 (m, 5H), 1.37 (s, 3H), 1.04 (t, J = 7.5 Hz, 3H). ^{13}C NMR (400 MHz, $CDCl_3$): δ 171.9 (s), 141.5 (s), 140.3 (s), 135.8 (s), 135.0 (s), 128.8 (s), 128.4 (s), 127.6 (s), 122.9 (s), 22.7 (s), 16.6 (s), 13.3 (s), 13.2 (s). UV–vis ($CHCl_3$): λ(nm) = 241 (ε = 18900 M^{-1} cm^{-1}), 295 (ε = 22800 $M^{-1}cm^{-1}$). EM-ES(+): ($C_{15}H_{17}NO$ + H) calcd 228.1388, found 228.1383. Observations: yellow solid.

*(Z)-3-Ethyl-4-methyl-5-(1-phenylethylidene)-1H-pyrrol-2(5H)-one (**Z-2a**).* ^{1}H NMR (400 MHz, $CDCl_3$): δ 7.42–7.22 (m, 1H), 6.90 (s, 1H), 2.41–2.33 (m, 2H), 2.30 (s, 1H), 1.09 (t, J = 7.5 Hz, 1H). ^{13}C NMR (400 MHz, $CDCl_3$): δ 170.1 (s), 141.8 (s), 139.5 (s), 136.1 (s), 134.2 (s), 128.8 (s), 127.8 (s), 127.7 (s), 121.4 (s), 19.9 (s), 16.5 (s), 14.4 (s), 13.4 (s). UV–vis ($CHCl_3$): λ(nm) = 306 (ε = 16600 M^{-1} cm^{-1}). EM-ES(+): ($C_{15}H_{17}NO$ + H) calcd 228.1388, found 228.1383.

*(E)-3-Ethyl-4-methyl-5-(1-(naphthalen-3-yl)ethylidene)-1H-pyrrol-2(5H)-one (**E-2b**).* Yield = 86% (0.2383 g, mp 147–148 °C). ^{1}H NMR (400 MHz, $CDCl_3$): δ 9.68 (s, 1H), 7.89–7.81 (m, 3H), 7.69 (s, 1H), 7.54–7.49 (m, 2H), 7.37 (d, J = 8.4 Hz, 1H), 2.39 (s, 3H), 2.33

DOI: 10.1021/acs.joc.6b00892
J. Org. Chem. 2016, 81, 6292–6302

(q, J = 7.4 Hz, 2H), 1.38 (s, 3H), 1.09 (t, J = 7.5 Hz, 3H). ^{13}C NMR (400 MHz, $CDCl_3$): δ 172.4 (s), 140.2 (s), 139.0 (s), 136.0 (s), 135.7 (s), 133.2 (s), 132.7 (s), 128.1 (s), 127.9 (s), 127.8 (s), 127.8 (s), 126.8 (s), 126.5 (s), 126.2 (s), 123.2 (s), 22.8 (s), 16.7 (s), 13.5 (s), 13.4 (s). UV−vis ($CHCl_3$): λ(nm) = 218 (ε = 42500 M^{-1} cm^{-1}), 280 (ε = 16500 M^{-1} cm^{-1}). EM-ES(+): ($C_{19}H_{19}NO$ + H) calcd 278.1545, found 278.1541. Observations: yellow solid.

*(E)-3-Ethyl-4-methyl-5-(1-(pyridin-2-yl)ethylidene)-1H-pyrrol-2(5H)-one (**E-2c**).* Yield = 52% (0.1186 g, mp 117−118 °C). ^{1}H NMR (400 MHz, $CDCl_3$): δ 8.64 (d, J = 4.8 Hz, 1H), 7.78 (s, 1H), 7.70 (t, J = 7.7 Hz, 1H), 7.30−7.27 (m, 1H), 7.25 (dd, J = 4.5, 3.1 Hz, 1H), 2.34−2.24 (m, 2H), 2.24 (s, 3H), 1.36 (s, 3H), 1.03 (t, J = 7.5 Hz, 3H). ^{13}C NMR (100 MHz, $CDCl_3$): δ 171.9 (s), 159.5 (s), 149.6 (s), 139.8 (s), 136.5 (s), 136.4 (s), 136.3 (s), 124.4 (s), 122.5 (s), 120.7 (s), 20.8 (s), 16.7 (s), 13.2 (s), 12.9 (s). UV−vis ($CHCl_3$): λ(nm) = 292 (ε = 15000 M^{-1} cm^{-1}). EM-ES(+): ($C_{14}H_{16}N_2O$ + H) calcd 229.1341, found 229.1345. Observations: yellow solid.

*(Z)-3-Ethyl-4-methyl-5-(1-(pyridin-2-yl)ethylidene)-1H-pyrrol-2(5H)-one (**Z-2c**).* Yield = 18% (0.0411 g). ^{1}H NMR (400 MHz, $CDCl_3$): δ 11.50 (d, J = 47.6 Hz, 1H), 8.58 (d, J = 4.7 Hz, 1H), 7.72 (t, J = 10.7, 5.3 Hz, 1H), 7.49 (d, J = 8.2 Hz, 1H), 7.14 (dd, J = 7.4, 4.9 Hz, 1H), 2.45−2.35 (m, 5H), 2.32 (s, 3H), 1.10 (t, J = 7.6 Hz, 3H). ^{13}C NMR (400 MHz, $CDCl_3$): δ 171.4 (s), 159.2 (s), 147.9 (s), 140.3 (s), 139.4 (s), 137.1 (s), 136.9 (s), 122.0 (s), 121.2 (s), 113.2 (s), 16.7 (s), 16.3 (s), 15.6 (s), 13.6 (s). UV−vis ($CHCl_3$): λ(nm) = 224 (ε = 11000 M^{-1} cm^{-1}), 344 (ε = 34500 M^{-1} cm^{-1}). EM-ES(+): ($C_{14}H_{16}N_2O$ + H): calcd 229.1341, found 229.1345. Observations: yellow solid.

■ ASSOCIATED CONTENT

Supporting Information

The Supporting Information is available free of charge on the ACS Publications website at DOI: 10.1021/acs.joc.6b00892.

UV−vis spectra, X-ray data, DOSY experiments, hydrogen-bond strength evaluation, irradiation time vs Z/E ratio plots, NMR spectra, and computational details (PDF)

X-ray data for **1d** (CIF)

X-ray data for **1f** (CIF)

X-ray data for **2c** (CIF)

■ AUTHOR INFORMATION

Corresponding Author

*E-mail: diego.sampedro@unirioja.es.

Notes

The authors declare no competing financial interest.

■ ACKNOWLEDGMENTS

This research was supported by the Spanish Ministerio de Ciencia e Innovación (MICINN)/Fondos Europeos para el Desarrollo Regional (FEDER) (CTQ2014-59650-P and CTQ2012-36966) and Project CCG2013/EXP-089 for the University of Alcalá (UAH). C.G.-I. thanks the Spanish MEC for her grant. Financial support by the Deutsche Forschungsgemeinschaft (GRK 2039) and KIT is gratefully acknowledged. We thank Fernando Rodríguez Royo for his help in resolving the X-ray structures.

■ REFERENCES

(1) Rockwell, N. C.; Lagarias, J. C. *ChemPhysChem* **2010**, *11*, 1172.
(2) Hoff, W. D.; Jung, K.-H.; Spudich, J. L. *Annu. Rev. Biophys. Biomol. Struct.* **1997**, *26*, 223.
(3) Bae, G.; Choi, G. *Annu. Rev. Plant Biol.* **2008**, *59*, 281.
(4) Cubitt, A. B.; Heim, R.; Adams, S. R.; Boyd, A. E.; Gross, L. A.; Tsien, R. Y. *Trends Biochem. Sci.* **1995**, *20*, 448.
(5) Liu, R. S. H. *Pure Appl. Chem.* **2002**, *74*, 1391.
(6) Lisenko, S. A.; Kugeiko, M. M. *J. Appl. Spectrosc.* **2014**, *81*, 834.
(7) Lightner, D. A.; Wooldridge, T. A.; McDonagh, A. F. *Biochem. Biophys. Res. Commun.* **1979**, *86*, 235.
(8) Sisson, T. R. *J. Invest. Dermatol.* **1981**, *77*, 158.
(9) Lamola, A. A.; Blumberg, W. E.; McClead, R.; Fanaroff, A. *Proc. Natl. Acad. Sci. U. S. A.* **1981**, *78*, 1882.
(10) Kandori, H.; Shichida, Y.; Yoshizawa, T. *Biochemistry (Moscow)* **2001**, *66*, 1197.
(11) Wu, L.; Burgess, K. *J. Am. Chem. Soc.* **2008**, *130*, 4089.
(12) Lopez, X.; Marques, M. A. L.; Castro, A.; Rubio, A. *J. Am. Chem. Soc.* **2005**, *127*, 12329.
(13) Borucki, B.; von Stetten, D.; Seibeck, S.; Lamparter, T.; Michael, N.; Mroginski, M. A.; Otto, H.; Murgida, D. H.; Heyn, M. P.; Hildebrandt, P. *J. Biol. Chem.* **2005**, *280*, 34358.
(14) Quail, P. H.; Boylan, M. T.; Parks, B. M.; Short, T. W.; Xu, Y.; Wagner, D. *Science* **1995**, *268*, 675.
(15) Essen, L.-O.; Mailliet, J.; Hughes, J. *Proc. Natl. Acad. Sci. U. S. A.* **2008**, *105*, 14709.
(16) Rohmer, T.; Lang, C.; Bongards, C.; Gupta, K. B. S. S.; Neugebauer, J.; Hughes, J.; Gartner, W.; Matysik, J. *J. Am. Chem. Soc.* **2010**, *132*, 4431.
(17) Rockwell, N. C.; Su, Y.-S.; Lagarias, J. C. *Annu. Rev. Plant Biol.* **2006**, *57*, 837.
(18) Nagy, F.; Schafer, E. *Annu. Rev. Plant Biol.* **2002**, *53*, 329.
(19) Kim, J.-I.; Song, P.-S. In *Light Sensing in Plants*; Springer, 2005; p 57.
(20) Hennig, L.; Stoddart, W. M.; Dieterle, M.; Whitelam, G. C.; Schäfer, E. *Plant Physiol.* **2002**, *128*, 194.
(21) Quail, P. H. *Annu. Rev. Genet.* **1991**, *25*, 389.
(22) Franklin, K. A.; Quail, P. H. *J. Exp. Bot.* **2010**, *61*, 11.
(23) Montgomery, B. L.; Lagarias, J. C. *Trends Plant Sci.* **2002**, *7*, 357.
(24) Smith, H. *Annu. Rev. Plant Physiol. Plant Mol. Biol.* **1995**, *46*, 289.
(25) McDonagh, A. F.; Palma, L. A.; Trull, F. R.; Lightner, D. A. *J. Am. Chem. Soc.* **1982**, *104*, 6865.
(26) Zunszain, P. A.; Ghuman, J.; McDonagh, A. F.; Curry, S. *J. Mol. Biol.* **2008**, *381*, 394.
(27) Le Bas, G.; Allegret, A.; Mauguen, Y.; De Rango, C.; Bailly, M. *Acta Crystallogr., Sect. B: Struct. Crystallogr. Cryst. Chem.* **1980**, *36*, 3007.
(28) Mreihil, K.; McDonagh, A. F.; Nakstad, B.; Hansen, T. W. R. *Pediatr. Res.* **2010**, *67*, 656.
(29) Ennever, J. F. *Photochem. Photobiol.* **1988**, *47*, 871.
(30) Vreman, H. J.; Wong, R. J.; Stevenson, D. K. *Semin Perinatol* **2004**, *28*, 326.
(31) McDonagh, A. F.; Palma, L. A.; Lightner, D. A. *Science* **1980**, *208*, 145.
(32) Lamola, A. A.; Flores, J.; Doleiden, F. H. *Photochem. Photobiol.* **1982**, *35*, 649.
(33) Gozem, S.; Melaccio, F.; Lindh, R.; Krylov, A. I.; Granovsky, A. A.; Angeli, C.; Olivucci, M. *J. Chem. Theory Comput.* **2013**, *9*, 4495.
(34) Ruckenbauer, M.; Barbatti, M.; Mueller, T.; Lischka, H. *J. Phys. Chem. A* **2013**, *117*, 2790.
(35) Chuang, W.-T.; Hsieh, C.-C.; Lai, C.-H.; Lai, C.-H.; Shih, C.-W.; Chen, K.-Y.; Hung, W.-Y.; Hsu, Y.-H.; Chou, P.-T. *J. Org. Chem.* **2011**, *76*, 8189.
(36) Hsieh, C.-C.; Chou, P.-T.; Shih, C.-W.; Chuang, W.-T.; Chung, M.-W.; Lee, J.; Joo, T. *J. Am. Chem. Soc.* **2011**, *133*, 2932.
(37) Vengris, M.; Van Stokkum, I. H. M.; He, X.; Bell, A. F.; Tonge, P. J.; van Grondelle, R.; Larsen, D. S. *J. Phys. Chem. A* **2004**, *108*, 4587.
(38) Wang, D.; Merz, T.; van Gunsteren, W. F. *Phys. Chem. Chem. Phys.* **2010**, *12*, 11051.
(39) Chepelev, L. L.; Beshara, C. S.; MacLean, P. D.; Hatfield, G. L.; Rand, A. A.; Thompson, A.; Wright, J. S.; Barclay, L. R. C. *J. Org. Chem.* **2006**, *71*, 22.
(40) Onkenhout, W.; Van Koeveringe, J. A.; Lugtenburg, J. *Recl. Trav. Chim. Pays-Bas* **1981**, *100*, 106.
(41) Park, Y.-T.; Hwang, J.-U. *Bull. Korean Chem. Soc.* **1980**, *1*, 23.

DOI: 10.1021/acs.joc.6b00892
J. Org. Chem. 2016, 81, 6292−6302

(42) Lightner, D. A.; Park, Y. T. *J. Heterocycl. Chem.* **1977**, *14*, 415.
(43) De Groot, J. A.; Jansen, H.; Fokkens, R.; Lugtenburg, J. *Recl.: J. R. Neth. Chem. Soc.* **1983**, *102*, 114.
(44) Huggins, M. T.; Billimoria, F. *J. Chem. Educ.* **2007**, *84*, 471.
(45) Huggins, M. T.; Musto, C.; Munro, L.; Catalano, V. J. *Tetrahedron* **2007**, *63*, 12994.
(46) Kessler, H. *Angew. Chem., Int. Ed. Engl.* **1982**, *21*, 512.
(47) Briand, J.; Bräm, O.; Réhault, J.; Léonard, J.; Cannizzo, A.; Chergui, M.; Zanirato, V.; Olivucci, M.; Helbing, J.; Haacke, S. *Phys. Chem. Chem. Phys.* **2010**, *12*, 3178.
(48) Léonard, J.; Schapiro, I.; Briand, J.; Fusi, S.; Paccani, R. R.; Olivucci, M.; Haacke, S. *Chem. - Eur. J.* **2012**, *18*, 15296.
(49) Léonard, J.; Briand, J.; Fusi, S.; Zanirato, V.; Olivucci, M.; Haacke, S. *New J. Phys.* **2013**, *15*, 105022.
(50) Renth, F.; Siewertsen, R.; Strübe, F.; Mattay, J.; Temps, F. *Phys. Chem. Chem. Phys.* **2014**, *16*, 19556.
(51) Bischoff, M.; Hermann, G.; Rentsch, S.; Strehlow, D. *Biochemistry* **2001**, *40*, 181.
(52) Schoenlein, R.; Peteanu, L.; Mathies, R.; Shank, C. *Science* **1991**, *254*, 412.
(53) Bongards, C.; Gaertner, W. *Photochem. Photobiol.* **2008**, *84*, 1109.
(54) Bongards, C.; Gartner, W. *Acc. Chem. Res.* **2010**, *43*, 485.
(55) Otwinowski, Z.; Minor, W. *Methods Enzymol.* **1997**, *276*, 307.
(56) Yang, J.-P.; Kappes, M.; Hippler, H.; Unterreiner, A.-N. *Phys. Chem. Chem. Phys.* **2005**, *7*, 512.
(57) Frick, E.; Ernst, H. A.; Voll, D.; Wolf, T. J.; Unterreiner, A.-N.; Barner-Kowollik, C. *Polym. Chem.* **2014**, *5*, 5053.
(58) Wolf, T. J.; Voll, D.; Barner-Kowollik, C.; Unterreiner, A.-N. *Macromolecules* **2012**, *45*, 2257.
(59) Kozma, I.; Baum, P.; Lochbrunner, S.; Riedle, E. *Opt. Express* **2003**, *11*, 3110.
(60) Riedle, E.; Beutter, M.; Lochbrunner, S.; Piel, J.; Schenkl, S.; Spörlein, S.; Zinth, W. *Appl. Phys. B: Lasers Opt.* **2000**, *71*, 457.
(61) Tomasi, J.; Mennucci, B.; Cammi, R. *Chem. Rev.* **2005**, *105*, 2999.
(62) Yanai, T.; Tew, D. P.; Handy, N. C. *Chem. Phys. Lett.* **2004**, *393*, 51.
(63) Frisch, M. J.; Trucks, G. W.; Schlegel, H. B.; Scuseria, G. E.; Robb, M. A.; Cheeseman, J. R.; Scalmani, G.; Barone, V.; Mennucci, B.; Petersson, G. A.; Nakatsuji, H.; Caricato, M.; Li, X.; Hratchian, H. P.; Izmaylov, A. F.; Bloino, J.; Zheng, G.; Sonnenberg, J. L.; Hada, M.; Ehara, M.; Toyota, K.; Fukuda, R.; Hasegawa, J.; Ishida, M.; Nakajima, T.; Honda, Y.; Kitao, O.; Nakai, H.; Vreven, T.; Montgomery, J. A., Jr.; Peralta, J. E.; Ogliaro, F.; Bearpark, M. J.; Heyd, J.; Brothers, E. N.; Kudin, K. N.; Staroverov, V. N.; Kobayashi, R.; Normand, J.; Raghavachari, K.; Rendell, A. P.; Burant, J. C.; Iyengar, S. S.; Tomasi, J.; Cossi, M.; Rega, N.; Millam, N. J.; Klene, M.; Knox, J. E.; Cross, J. B.; Bakken, V.; Adamo, C.; Jaramillo, J.; Gomperts, R.; Stratmann, R. E.; Yazyev, O.; Austin, A. J.; Cammi, R.; Pomelli, C.; Ochterski, J. W.; Martin, R. L.; Morokuma, K.; Zakrzewski, V. G.; Voth, G. A.; Salvador, P.; Dannenberg, J. J.; Dapprich, S.; Daniels, A. D.; Farkas, Ö.; Foresman, J. B.; Ortiz, J. V.; Cioslowski, J.; Fox, D. J. *Gaussian 09*; Gaussian, Inc.: Wallingford, CT, 2009.

DOI: 10.1021/acs.joc.6b00892
J. Org. Chem. 2016, 81, 6292−6302